Letter

Dipolar Weyl semimetals

Alexander C. Tyner[1,*] and Shouvik Sur[2]

[1]*Graduate Program in Applied Physics, Northwestern University, Evanston, Illinois 60208, USA*

[2]*Department of Physics and Astronomy, Rice Center for Quantum Materials, Rice University, Houston, Texas 77005, USA*

(Received 9 April 2023; accepted 2 January 2024; published 2 February 2024)

In Weyl semimetals, Weyl points act as monopoles and antimonopoles of the Berry curvature, with a monopole-antimonopole pair producing a net-zero Berry flux. When inversion symmetry is preserved, the two-dimensional (2D) planes that separate a monopole-antimonopole pair of Weyl points carry quantized Berry flux. In this work, we introduce a class of symmetry-protected Weyl semimetals which host monopole-antimonopole pairs of Weyl points that generate a dipolar Berry flux. Thus, both monopolar and dipolar Berry fluxes coexist in the Brillouin zone, which results in two distinct types of topologically nontrivial planes separating the Weyl points, carrying either a quantized monopolar or a quantized dipolar flux. We construct a topological invariant—the staggered Chern number—to measure the latter, and employ it to topologically distinguish between various Weyl points. Finally, through a minimal two-band model, we investigate physical signatures of bulk topology, including surface Fermi arcs, zero-energy hinge states, and response to insertion of a π-flux vortex.

DOI: 10.1103/PhysRevB.109.L081101

Introduction. Weyl semimetals (WSMs) constitute the most well-known class of topological semimetals which has guided the exploration of other topological semimetallic phases [1–21]. The fact that band-crossing points or Weyl points (WPs) are monopoles of the Berry curvature is one of the most remarkable features of WSMs [1,22]. Arguably, inversion-symmetric WSMs offer the simplest realization of three-dimensional topological semimetals. In these systems, the two-dimensional planes separating a pair of WPs, carrying opposite Berry-monopole charges, are classified as Chern insulators. The Weyl points, respectively, act as source and sink of the quantized Berry flux passing through the Chern planes. Furthermore, the edge states supported by each Chern insulating layer stack up to give rise to the chiral Fermi-arc states on the surface of WSMs. These notions have been generalized by the discovery of higher-order WSMs, where all topologically nontrivial planes are not Chern insulators, and both Fermi-arc surface states and hinge-localized zero modes are present at crystal terminations [23–26].

Recently, Nelson *et al.* [27] have shown that the topological critical point separating Hopf and ordinary insulators realizes a Berry *dipole*, which asymptotically act as both a source and a sink of Berry curvature. In contrast to a WP, the net Berry flux penetrating a Gaussian surface (GS) enclosing a Berry dipole vanishes. Instead, the flux is staggered on the GS, with its sign determined by the orientation of the dipole relative to local normals on the GS. Therefore, in a hypothetical semimetal, hosting at least a pair of Berry dipoles, one may expect that the planes separating the dipoles would be threaded by a staggered or dipolar Berry flux. Are these "dipolar planes" topologically nontrivial, and, importantly, does the notion of Berry dipoles lead to hitherto unexplored classes of WSMs?

In this Letter, we introduce a class of symmetry-protected WSMs, coined "dipolar Weyl semimetals," where Chern, dipolar, and ordinary insulating planes coexist, as summarized in Fig. 1(a). The WPs in such WSMs result from splitting Berry dipoles, which distinguishes dipolar WSMs from both conventional and higher-order WSMs [see Fig. 1(b)]. We construct two-band models for describing dipolar WSMs, and show that dipolar planes support a quantized, but staggered, Berry flux, as exemplified by Fig. 1(c). Therefore, the WPs occurring at the boundary between dipolar and Chern insulators are distinguished from that at the boundary between Chern and ordinary insulators. Remarkably, on surface terminations perpendicular to the separation between WPs, both chiral Fermi-arc states and hinge-localized zero modes are realized. In order to characterize the bulk topology, we determine the response of the bulk states to π-flux vortex insertions, and applied magnetic fields. In spite of its similarity to higher-order WSMs [23,24], we note that dipolar WSMs require only two bands, such that its bulk topology is completely determined by the bands that cross at the WPs.

Model and phase diagram. We consider two-band models of WSMs protected by a combination of n-fold improper rotational (or rotoreflection) symmetry $\mathcal{S}^z_m = \mathcal{M}_z \circ \mathcal{C}^z_m$, and two antiunitary mirror symmetries ($\mathcal{M}_1$ and $\mathcal{M}_2$). Here, $\mathcal{M}_z$ is the mirror operator that sends $z \to -z$, and $\mathcal{C}^z_m$ generates m-fold rotations about the $\hat{z}$ axis. We begin with the single-particle Hamiltonian

$$H(\boldsymbol{k}) = \sum_{j=1}^{3} n_j(\boldsymbol{k})\sigma_j, \tag{1}$$

where σ_j is the jth Pauli matrix, $n_1 = 2(u_4u_1 + u_3u_2)$, $n_2 = 2(u_4u_2 - u_3u_1)$, and $n_3 = u_4^2 + u_3^2 - u_1^2 - u_2^2$. We require (u_1, u_2) [u_3 and u_4] to transform under an E [B and A,

*Present address: Nordita, KTH Royal Institute of Technology and Stockholm University 106 91 Stockholm, Sweden

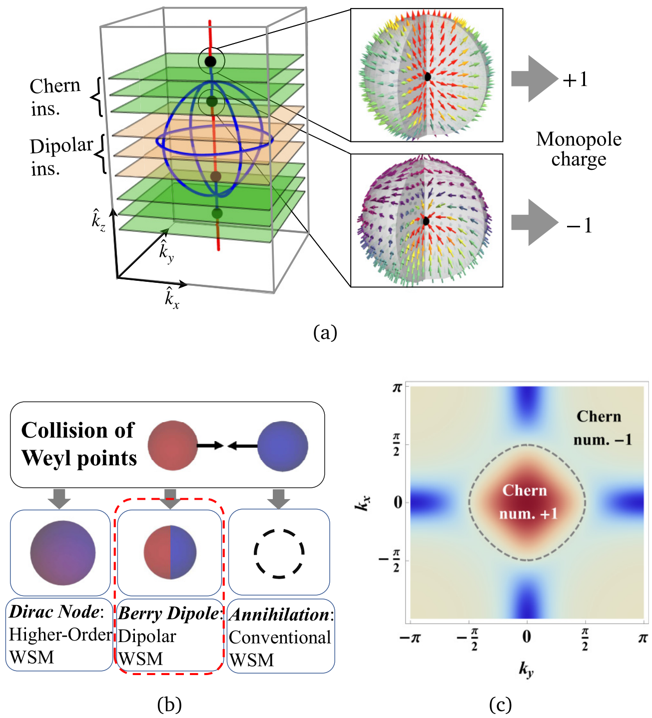

FIG. 1. Properties of the dipolar Weyl semimetal (WSM) phase. (a) Four Weyl points (WPs) (black spheres) occur on the rotation axis, with alternating monopole charges. The sign is deduced by visualizing the Berry curvature $\boldsymbol{\mathcal{B}}$ in the vicinity of the WPs (right). Depending on their location relative to the WPs, the 2D planes layered along $\hat{k}_z$ are either dipolar (red), Chern (green), or ordinary (unmarked) insulators. The red (blue) curves indicate points in the Brillouin zone that map to $\hat{n} = \vec{n}/|\vec{n}| = (0,0,1)$ [$(0,0,-1)$], where $\hat{n}$ is defined in Eq. (1). The intersection of these curves along the rotation axis marks the locations of band inversion (black spheres). (b) In dipolar (higher-order [23]) WSMs, there exist pairs of WPs with monopolecharge ± 1 whose collision leads to a Berry dipole (Dirac point). In conventional WSMs, any monopole-antimonopole pair of WPs annihilate upon collision. (c) On the dipolar insulating planes the distribution of $\mathcal{B}_z$ (color profile) is such that two Chern insulators, with opposite Chern numbers, are embedded within the same plane. In Eq. (4), we define the notion of "staggered Chern number" to succinctly capture this pattern.

respectively] representation of $\mathcal{C}_m^z$, and $\{u_1, u_2, u_4\}$ [u_3] to be even [odd] under $\mathcal{M}_z$. Consequently, (n_1, n_2) [n_3] transform under an E [A] representation of $\mathcal{S}_m^z$. Since n_j's do not yet have the most general symmetry-allowed form, we modify them as $n_j \to n_j + \nu_j$, where ν_j's will be considered as symmetry-allowed perturbations. Under $\mathcal{S}_m^z$, the Hamiltonian transforms covariantly:

$$\mathcal{S}_m^z H(\boldsymbol{k}) \left(\mathcal{S}_m^z\right)^{-1} = H(\boldsymbol{k}') = U^\dagger H(\boldsymbol{k}) U, \tag{2}$$

where $\boldsymbol{k}' = (\mathfrak{R}_m \boldsymbol{k}_\perp, -k_z)$ with $\boldsymbol{k}_\perp = (k_x, k_y)$, $\mathfrak{R}_m$ implements m-fold rotation about $\hat{k}_z$, and $U = \exp[-\frac{i\pi}{m}\sigma_3]$. Therefore, $[H(\boldsymbol{k}), \mathcal{S}_m^z] = 0$ at high-symmetry points (HSPs) that satisfy $\boldsymbol{k}' \equiv \boldsymbol{k}$. Because of the constraints placed on u_j's and ν_j's by $\mathcal{S}_m^z$, $n_{j=1,2}$ must vanish both at the HSPs and along the rotation axis. The remaining component n_3 is finite in general, and it may change sign between a pair of HSPs only if $u_4^2 + \nu_3$ does not have a fixed sign throughout the Brillouin zone (BZ) [28]. While the rotoreflection symmetry guarantees a parameter window where the bands cross along the rotation axis, the antiunitary mirror symmetries protect quantized one-dimensional (1D) polarizations along orthogonal high-symmetry axes.

For concreteness, we focus on $m = 4$, and choose

$$\frac{u_1}{t_p} = \sin k_x, \quad \frac{u_2}{t_p} = \sin k_y, \quad \frac{u_3}{t_d} = \sin k_z(\cos k_y - \cos k_x),$$
$$u_4 = t_s\{\Delta - (\cos k_x + \cos k_y + \gamma \cos k_z)\},$$
$$\nu_1 = 2t_s t_p \delta_\perp \sin k_x; \quad \nu_2 = 2t_s t_p \delta_\perp \sin k_y; \nu_3 = -t_s^2 \delta_3^2. \tag{3}$$

Here, $\{t_p, t_d, t_s, \Delta, \delta_\perp, \delta_z, \gamma\}$ are model parameters. We note that, at the critical points obtained by setting all $\nu_j = 0$, the Hamiltonian reduces to a form that may be obtained from a model of Dirac semimetal (DSM) with a $\mathbb{Z}_2$-chiral symmetry, $h(\mathbf{k}) = \vec{u} \cdot \vec{\Gamma}$ with Γ_j's being a set of four mutually anticommuting matrices, by following the "Hopf mapping" procedure in Ref. [29]. The antiunitary mirror symmetries act as $\mathcal{M}_1 H(\boldsymbol{k}) \mathcal{M}_1^{-1} \equiv H^*(-k_+, k_-, k_z) = e^{-i\frac{\pi}{4}\sigma_3} H(\boldsymbol{k}) e^{i\frac{\pi}{4}\sigma_3}$ and $\mathcal{M}_2 H(\boldsymbol{k}) \mathcal{M}_2^{-1} \equiv H^*(k_+, -k_-, k_z) = e^{i\frac{\pi}{4}\sigma_3} H(\boldsymbol{k}) e^{-i\frac{\pi}{4}\sigma_3}$, where $k_\pm = \frac{1}{\sqrt{2}}(k_x \pm k_y)$. For simplicity, henceforth, we set $(\gamma, \delta_\perp) = (1, 0)$ and $\Delta, \delta_3 \geqslant 0$, and note that relaxing these constraints does not qualitatively alter our conclusions.

In the BZ of a tetragonal lattice, $[H, \mathcal{S}_4^z] = 0$ at $\Gamma \equiv (0,0,0)$, $Z \equiv (0,0,\pi)$, $M \equiv (\pi,\pi,0)$, and $A \equiv (\pi,\pi,\pi)$ points. Bands invert with respect to $\mathcal{S}_4^z$ around the Γ (Z) point for $\delta_3 > |\Delta - 3|$ ($\delta_3 > |\Delta - 1|$). As shown in Fig. 2(a), in these regions conventional Weyl semimetallic phases are realized. Since n_3 obtains the same sign at *all* HSPs for $(1 + \delta_3) < \Delta < (3 - \delta_3)$, no band inversion would be detected by comparing the eigenvalues of $\mathcal{S}_4^z$ at these points. Thus, it may appear that in this parameter regime the system is topologically trivial. This is false, however, because along the Γ-Z line we identify *two* locations of band inversion with respect to $\mathcal{S}_4^z$ at non-HSPs, as shown in Fig 1(a). We refer to these points as "hidden" band inversions, since their existence cannot be deduced by consulting the HSPs alone. What are the ramifications of such "hidden" band inversions?

Dipolar Weyl semimetal. In d dimensions, nontrivial topology can be deduced from the texture of $\hat{n}(\boldsymbol{k})$. In particular, $\hat{n}(\boldsymbol{k})$ maps the d-dimensional BZ (T^d) to the 2-sphere (S^2) as a function of $\boldsymbol{k}$. Valuable insights are obtained by consulting the set of points in the BZ which get mapped to a single point on S^2 by $\hat{n}(\boldsymbol{k})$ [i.e., the preimages $\hat{n}(\boldsymbol{k})$]. In analogy to Hopf insulators [29], the preimages of individual points on S^2 are 1D curves in the three-dimensional BZ for the dipolar WSMs. In contrast to Hopf insulators, however, the preimages of two distinct points on S^2 are not necessarily linked in dipolar WSMs. Thus, the linking number or Hopf invariant vanishes. In the DWSM phase, the preimages of the "north" (red) and "south" (blue) poles of S^2—defined by the simultaneous vanishing of n_1 and n_2 with $\hat{n}_3 = \pm 1$, respectively—intersect at $k_z = \pm \cos^{-1}(\Delta - 2 \pm \delta_3)$ along the Γ-Z line, as shown in Fig. 1(a). Since $H(\boldsymbol{k})$ commutes with $\mathcal{S}_4^z$ on the polar preimages, these intersections are locations of band inversions with respect to $\mathcal{S}_4^z$. The existence of the intersections is symmetry protected, and remains robust

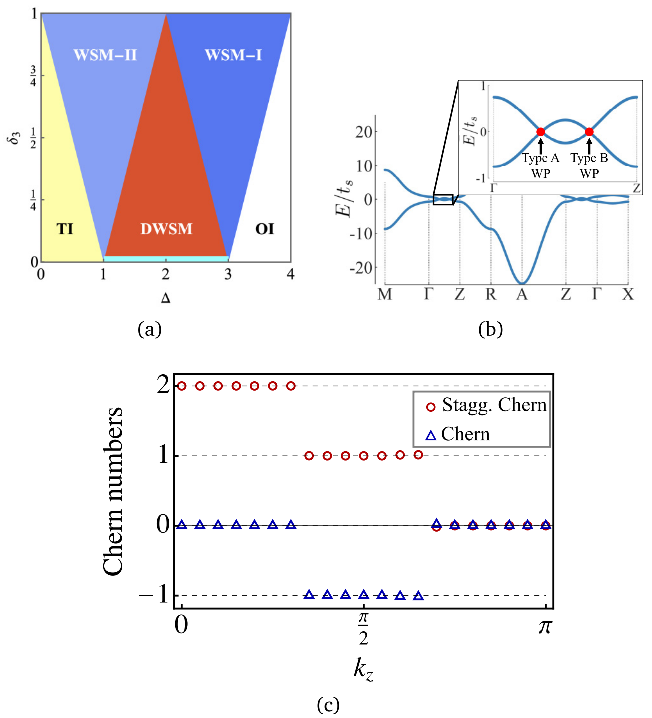

FIG. 2. Characterization of the phases supported by $H(\boldsymbol{k})$. (a) Phase diagram. A dipolar Weyl semimetal (DWSM) phase exists in the range $(1+\delta_3) < \Delta < (3-\delta_3)$, while conventional WSM phases (WSM-I and WSM-II) are found when $\delta_3 > |\Delta - 1|$ and $\delta_3 > |\Delta - 3|$. Here, TI (OI) indicate topological (ordinary) insulating phases. At $\delta_3 = 0$ and $1 < \Delta < 3$ the Weyl points in the DWSM merge on either side of the k_z axis, thereby forming Berry dipoles [cf. Fig. 1(b)]. These critical points are marked in cyan. (b) Band structure in the DWSM phase along high-symmetry paths in a tetragonal Brillouin zone. Four Weyl points occur along the Γ-Z axis. These are classified into two categories (A and B) based on the type of 2D insulating planes they separate [see (c)]. (c) Distribution of the Chern and staggered Chern numbers carried by (k_x, k_y) planes, as a function of k_z.

against $\delta_\perp$ as long as $|\delta_\perp| < \delta_3$. Because $\vec{n}(\boldsymbol{k}) = \vec{0}$ at the intersection of the preimages of the north and south poles, these locations correspond to the Weyl points [see Fig. 2(b)].

Topology of bulk states. By enclosing the band-crossing points by GSs, we determine the net Berry flux emanating from these band singularities to be 2π up to an overall sign, as illustrated in Fig. 1(a). Therefore, the band-crossing points are unit-strength monopoles of the Berry curvature, and we identify them as WPs. When a GS encloses both WPs on a fixed side of the k_z axis, the net Berry flux passing through this surface vanishes. The region within the GS is topologically nontrivial, however, as a nonzero net Berry *dipole flux* pierces the surface. The existence of the dipole flux can be understood by appealing to the topological critical point at $(\delta_3, \delta_\perp) = (0, 0)$: as $\delta_3 \to 0$, the pair of WPs at $|k_z| = \cos^{-1}(\Delta - 2 \pm \delta_3)$ collide to yield a pair of band singularities at $|k_z| = \cos^{-1}(\Delta - 2)$, which act as sources of the dipole flux [i.e., Berry dipoles; see Fig. 1(b)]. On an infinitesimal GS enclosing the latter band-crossing points, the Berry flux obtains a staggered form with the northern (southern) hemisphere supporting a 2π (-2π) net flux. Thus, for $\delta_3 > 0$, when a Gaussian surface encloses the monopole-antimonopole pair at $|k_z| = \cos^{-1}(\Delta - 2 \pm \delta_3)$, a net dipole flux survives. This unusual behavior of the WPs in dipolar WSMs is summarized with further details in Sec. II D of the Supplemental Material (SM) [30]. The presence of both monopole and dipole fluxes indicates that topologically nontrivial k_z planes in the BZ are not limited to being 2D Chern insulators.

Indeed, the k_z planes between $k_z = \pm\cos^{-1}(\Delta - 2 + \delta_3)$ [red planes in Fig. 1(a)] support a dipolar version of the Berry flux which reflects the presence of a skyrmionium texture [31] for $\vec{n}(\boldsymbol{k})$. Skyrmioniums are composed of two oppositely charged but nonoverlapping skyrmions; consequently, they do not support a finite Chern number. It is possible to define a quantized topological invariant, however, that distinguishes a skyrmionium-carrying plane from an ordinary 2D insulator. In order to emphasize its origin in a staggered distribution of Berry curvature on the $\boldsymbol{k}_\perp$ plane, we call this topological invariant "staggered Chern number," and define it as

$$\mathfrak{C}_{\rm stagg}(k_z) = \frac{1}{2\pi}\int d\boldsymbol{k}_\perp \mathcal{B}_z(\boldsymbol{k}_\perp, k_z) f_{\rm stagg}(\boldsymbol{k}_\perp), \tag{4}$$

where $\mathcal{B}_z(\boldsymbol{k}_\perp, k_z)$ is the $\hat{k}_z$ component of the Berry curvature, and $f_{\rm stagg}(\boldsymbol{k}_\perp)$ is a weight function that is determined by $H(\boldsymbol{k})$ such that $\int d\boldsymbol{k}_\perp f_{\rm stagg}(\boldsymbol{k}_\perp) = 0$. Since $\mathfrak{C}_{\rm stagg}$ is effectively the difference of Chern numbers of the same magnitude but opposite signs, it equals the Chern number when the staggering is absent. If a quantized staggering of flux is present, then $\mathfrak{C}_{\rm stagg}$ will be an even integer, in analogy to familiar mirror [32] or spin [33] Chern numbers. While on mirror- or spin-Chern number carrying planes the Chern number is staggered in an internal subspace, here, it is staggered in the momentum space. An alternative formulation of $\mathfrak{C}_{\rm stagg}$ that does not require an explicit knowledge of $f_{\rm stagg}$, but utilizes effective Su-Schrieffer-Heeger [34] forms of the Hamiltonian on the mirror axes, is provided in Sec. II B the SM [30].

We plot $\mathfrak{C}_{\rm stagg}$ as a function of k_z in Fig. 2(c), and relegate the details of the calculation to the SM [30], along with the explicit form of $f_{\rm stagg}(\boldsymbol{k}_\perp)$. We obtain $\mathfrak{C}_{\rm stagg} = 2$ for all planes with $|k_z| < \cos^{-1}(\Delta - 2 + \delta_3)$, indicating intertwining of two regions with opposite Chern numbers. We note that the $k_z = 0$ and π planes of the dipolar WSM are identical to respective planes in the Moore-Ran-Wen class of models of Hopf insulators [29]. Consequently, these special planes in Hopf insulators are also characterized by a quantized staggered-Chern number. The staggering of the Chern number in dipolar WSMs, as well as Hopf insulators, originates from nontrivial 2D winding numbers supported by corresponding $\boldsymbol{k}_\perp$ planes of the system governed by $h(\boldsymbol{k}) = \vec{u} \cdot \vec{\Gamma}$. In the present case, $h(\boldsymbol{k})$ describes a $\mathbb{Z}_2$-chiral DSM with a pair of band-crossings along the k_z axis. The k_z planes lying between the Dirac points are characterized by the relative-Chern number [35], which is a $\mathbb{Z}$-valued 2D bulk invariant and a variant of the spin-Chern number, and it is protected by both bulk and spin gaps [36,37]. The nontrivial $\mathfrak{C}_{\rm stagg}$ is thus a manifestation of the nontrivial relative- or spin-Chern number supported by the k_z planes of chiral DSMs [35]. Thus, under the Hopf map, the staggering of the Chern number in a Kramers degenerate subspace maps to its staggering in momentum space.

The k_z planes separating WPs on the *same* side of the k_z axis, i.e., $\cos^{-1}(\Delta - 2 + \delta_3) < |k_z| < \cos^{-1}(\Delta - 2 - \delta_3)$

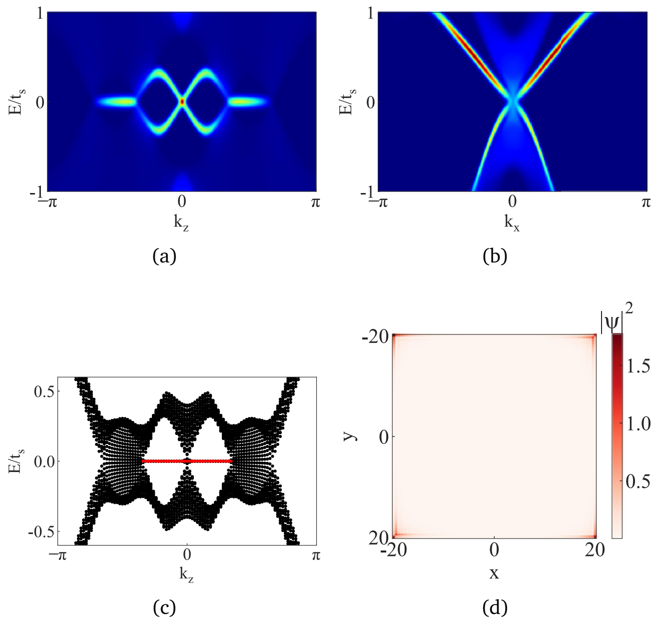

FIG. 3. Spectra of surface and hinge localized states. (a) Spectral density on the (100) surface as a function of k_z. Zero energy Fermi arcs are present between projections of the Weyl points on the same side of the k_z axis. The central region supports a dispersive, nondegenerate, Dirac conelike feature centered at the $\bar{\Gamma}$ point of the surface Brillouin zone. (b) Spectra on (001) surface as a function of k_x fixing $k_y = 0$, displaying a Dirac cone without a band-crossing point. (c) Spectrum from exact diagonalization with periodic boundary condition only along $\hat{z}$. The dispersionless midgap states (marked in red) are localized at the corners of the (x, y) planes, shown in (d), thereby forming dispersionless hinge modes.

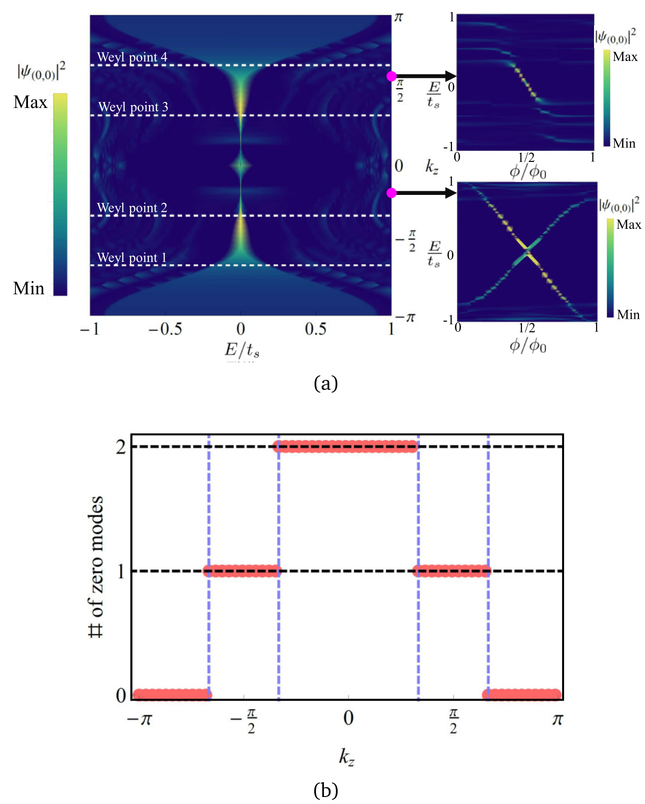

FIG. 4. Vortex-bound states as a diagnostic of bulk topology. (a) Probability density (PD) at the location of vortex for 120 states closest to zero energy. Left: PD for vortex flux $\phi = \phi_0/2$ as a function of energy and k_z. Here, ϕ_0 is the quantum of flux. Zero modes exist for *all* topologically nontrivial planes. Right: PD as a function of ϕ and energy, fixing k_z. Both Chern (top right) and staggered-Chern planes (bottom right) support charge pumping. (b) Number of vortex-bound zero modes upon insertion of magnetic flux tube with $\phi = \phi_0/2$. The distinct number of zero modes establishes the different topological character of $\boldsymbol{k}_\perp$ planes as a function of k_z.

[green planes in Fig. 1(a)], carry a Chern number $\mathfrak{C} = -1$, as shown in Fig. 2(c). By contrast, all planes with $|k_z| > \cos^{-1}(\Delta - 2 - \delta_3)$ are topologically trivial with $\mathfrak{C}_{\rm stagg} = 0 = \mathfrak{C}$. Thus, the k_z plane hosting a type-A (-B) WP [see inset in Fig. 2(b)] may be interpreted as the topological critical point separating a staggered-Chern and a Chern insulator (a Chern and an ordinary insulator). Here, while the k_z plane hosting a type-B WP supports a half-integer Chern and staggered-Chern number of equal magnitude, the k_z plane hosting type-A WP supports a half-integer Chern number and a *distinct* half-integer staggered Chern number [30].

Surface and hinge states. The states on the (100) and (010) surfaces are sensitive to the texture of $\hat{n}(\boldsymbol{k})$ in the bulk. As a representative example, we portray the topologically protected states on the (100) surface in Fig. 3(a). Fermi arcs are found to connect the projections of WPs on the same side of the k_z axis, indicating their origin in the nontrivial Chern insulating planes. The staggered-Chern or dipolar planes have a distinct topological response to surface terminations, which is reminiscent of *sp*-Dirac semimetals [35,38]. In particular, generic dipolar planes support a pair of gapped edge states. On the $k_z = 0$ (and π) plane $\mathcal{S}_4^z$ reduces to $\mathcal{C}_4^z$, which allows it to support gapless edge states. This leads to the single copy of Dirac cone centered at the $\bar{\Gamma}$ point of the surface BZ. The pair of degenerate surface states at the $\bar{\Gamma}$ point is protected by a quantized 1D winding number in the bulk along the k_x axis [30]. The states on the (001) surface exist as long as the $\mathcal{S}_4^z$ symmetry is preserved. As shown in Fig. 3(b), these states form a Dirac conelike feature about the zone center of the (001) surface BZ, with the band-crossing point absent. The center of the (001) surface BZ corresponds to the projection of the rotation axis, which accounts for the lack of normalizability at this point [35].

While generic k_z planes in the region $|k_z| < \cos^{-1}(\Delta - 2 + \delta_3)$ support gapped edge states, they also support corner-localized zero modes, which are protected by the antiunitary mirror symmetries. These corner localized modes stack along the $\hat{z}$ direction to give rise to hinge localized zero modes. In Figs. 3(c) and 3(d) we identify these hinge states by exactly diagonalizing the Hamiltonian with periodic boundary condition only along $\hat{z}$. In Sec. III of the SM [30] (also see Ref. [39]) we detail the presence of a quantized, one-dimensional winding number along the diagonal axes, which protect the corner localized zero modes in accordance with Ref. [40]. Thus, surface- and hinge-localized Fermi arcs are simultaneously present in dipolar WSMs, which is reminiscent of higher-order topological semimetals [23,24,35,41].

Vortex-bound states. In the position space, field-theoretical calculations have proven that the bulk topological invariant in the ground state can be computed through insertion of an electromagnetic π-flux vortex. In particular, the number of states bound to the vortex corresponds to the magnitude of the quantized flux in the ground state of a 2D topological insulator [35,42–46]. Moreover, as the magnitude of flux carried by the vortex is tuned between zero and the flux quanta $\phi_0 = h/e$, the vortex-bound modes are pumped across the bulk band gap.

To unambiguously examine the topological response of the two-dimensional planes stacked along $\hat{k}_z$, we consider them as independent layers of 2D insulators, labeled by k_z. In the position space for each layer, we insert a vortex tube at the origin, carrying a flux ϕ. We exactly diagonalize the resultant Hamiltonian on a 20×20 lattice, which yields a k_z-dependent energy spectrum, as shown in Fig. 4(a). The unit strength Chern planes at $\cos^{-1}(\Delta - 2 + \delta_3) < |k_z| < \cos^{-1}(\Delta - 2 - \delta_3)$ support a single vortex-bound state, which is pumped across the bulk band gap as a function of ϕ. The dipolar or staggered-Chern planes at $|k_z| < \cos^{-1}(\Delta - 2 + \delta_3)$ support *two* states at the vortex, each corresponding to a Chern sector. Since the Chern sectors carry opposite Chern numbers, these vortex-bound states are pumped in opposite directions as a function of ϕ, reminiscent of spin-Hall insulators [42,43,47,48]. Importantly, as demonstrated in Fig. 4(b), when the strength of flux is held fixed at $\phi = \phi_0/2$, the number of vortex-bound modes can be used as a quantized diagnostic of the topology of the 2D layers. Since both $\mathfrak{C}_{\text{stagg}}$ and the number of vortex-bound zero modes effectively count the number of Chern sectors in each layer, they have an identical response [cf. Figs. 2(b) and 4(b)].

Conclusion. We introduced a class of WSMs where both dipole- and monopole-flux carrying planes are present. A topological invariant, the staggered Chern number, is formulated for diagnosing the presence of quantized dipolar flux. Through flux insertions, the dipolar planes are shown to have a topological response that is analogous to generalized spin-Hall insulators. With the help of a two-band model, we demonstrated that surface and hinge states are reminiscent of higher-order topological semimetals. A detailed comparison among dipolar, higher-order, and conventional WSMs is presented in the SM [30], where we show that the clearest distinction between a dipolar and a higher-order WSM arises in the Landau level spectra.

The two-band model discussed here follows a similar principle of construction as Hopf insulators. Therefore, we expect it would be possible to simulate it within the same platforms proposed for realizing the latter [49–55]. Further, it is possible to construct variants of the same model, with potentially more exotic topological singularities [56–59]. Both considerations are left to future works.

Acknowledgments. A.C.T. was supported by the startup funds of Pallab Goswami at Northwestern University and the National Science Foundation MRSEC program (Grant No. DMR-1720139) at the Materials Research Center of Northwestern University. S.S. was supported in parts by the DOE DE-SC0020177, and National Science Foundation under Grant No. DMR-2220603. We thank the anonymous referee for helpful comments which has improved the quality of this work.

[1] X. Wan, A. M. Turner, A. Vishwanath, and S. Y. Savrasov, Topological semimetal and Fermi-arc surface states in the electronic structure of pyrochlore iridates, Phys. Rev. B **83**, 205101 (2011).

[2] K.-Y. Yang, Y.-M. Lu, and Y. Ran, Quantum Hall effects in a Weyl semimetal: Possible application in pyrochlore iridates, Phys. Rev. B **84**, 075129 (2011).

[3] A. A. Burkov and L. Balents, Weyl semimetal in a topological insulator multilayer, Phys. Rev. Lett. **107**, 127205 (2011).

[4] A. A. Burkov, M. D. Hook, and L. Balents, Topological nodal semimetals, Phys. Rev. B **84**, 235126 (2011).

[5] C. Fang, M. J. Gilbert, X. Dai, and B. A. Bernevig, Multi-Weyl topological semimetals stabilized by point group symmetry, Phys. Rev. Lett. **108**, 266802 (2012).

[6] G. B. Halász and L. Balents, Time-reversal invariant realization of the Weyl semimetal phase, Phys. Rev. B **85**, 035103 (2012).

[7] A. A. Zyuzin and A. A. Burkov, Topological response in Weyl semimetals and the chiral anomaly, Phys. Rev. B **86**, 115133 (2012).

[8] M. M. Vazifeh and M. Franz, Electromagnetic response of Weyl semimetals, Phys. Rev. Lett. **111**, 027201 (2013).

[9] P. Goswami and S. Tewari, Axionic field theory of (3 + 1)-dimensional Weyl semimetals, Phys. Rev. B **88**, 245107 (2013).

[10] P. Hosur and X. Qi, Recent developments in transport phenomena in Weyl semimetals, C. R. Phys. **14**, 857 (2013).

[11] J. Liu and D. Vanderbilt, Weyl semimetals from noncentrosymmetric topological insulators, Phys. Rev. B **90**, 155316 (2014).

[12] B. Q. Lv, H. M. Weng, B. B. Fu, X. P. Wang, H. Miao, J. Ma, P. Richard, X. C. Huang, L. X. Zhao, G. F. Chen, Z. Fang, X. Dai, T. Qian, and H. Ding, Experimental discovery of Weyl semimetal TaAs, Phys. Rev. X **5**, 031013 (2015).

[13] S.-Y. Xu, I. Belopolski, N. Alidoust, M. Neupane, G. Bian, C. Zhang, R. Sankar, G. Chang, Z. Yuan, C.-C. Lee *et al.*, Discovery of a Weyl fermion semimetal and topological Fermi arcs, Science **349**, 613 (2015).

[14] L. X. Yang, Z. K. Liu, Y. Sun, H. Peng, H. F. Yang, T. Zhang, B. Zhou, Y. Zhang, Y. F. Guo, M. Rahn *et al.*, Weyl semimetal phase in the non-centrosymmetric compound TaAs, Nat. Phys. **11**, 728 (2015).

[15] S.-Y. Xu, I. Belopolski, D. S. Sanchez, C. Zhang, G. Chang, C. Guo, G. Bian, Z. Yuan, H. Lu, T.-R. Chang *et al.*, Experimental discovery of a topological Weyl semimetal state in TaP, Sci. Adv. **1**, e1501092 (2015).

[16] H. Weng, C. Fang, Z. Fang, B. A. Bernevig, and X. Dai, Weyl semimetal phase in noncentrosymmetric transition-metal monophosphides, Phys. Rev. X **5**, 011029 (2015).

[17] Y. Sun, S.-C. Wu, M. N. Ali, C. Felser, and B. Yan, Prediction of Weyl semimetal in orthorhombic $MoTe_2$, Phys. Rev. B **92**, 161107(R) (2015).

[18] A. A Soluyanov, D. Gresch, Z. Wang, QuanSheng Wu, M. Troyer, X. Dai, and B. A. Bernevig, Type-II Weyl semimetals, Nature (London) **527**, 495 (2015).

[19] S. Jia, S.-Y. Xu, and M. Z. Hasan, Weyl semimetals, Fermi arcs and Chiral anomalies, Nat. Mater. **15**, 1140 (2016).

[20] B. Yan and C. Felser, Topological materials: Weyl semimetals, Annu. Rev. Condens. Matter Phys. **8**, 337 (2017).

[21] N. P. Armitage, E. J. Mele, and A. Vishwanath, Weyl and Dirac semimetals in three-dimensional solids, Rev. Mod. Phys. **90**, 015001 (2018).
[22] G. E. Volovik, Zeros in the fermion spectrum in superfluid systems as diabolical points, JETP Lett **46**, 81 (1987).
[23] S. A. A. Ghorashi, T. Li, and T. L. Hughes, Higher-order Weyl semimetals, Phys. Rev. Lett. **125**, 266804 (2020).
[24] H.-X. Wang, Z.-K. Lin, B. Jiang, G.-Y. Guo, and J.-H. Jiang, Higher-order Weyl semimetals, Phys. Rev. Lett. **125**, 146401 (2020).
[25] B. Xie, H. Liu, H. Cheng, Z. Liu, J. Tian, and S. Chen, Dirac points and the transition towards Weyl points in three-dimensional sonic crystals, Light Sci. Appl. **9**, 201 (2020).
[26] L. Luo, H.-X. Wang, Z.-K. Lin, B. Jiang, Y. Wu, F. Li, and J.-H. Jiang, Observation of a phononic higher-order Weyl semimetal, Nat. Mater. **20**, 794 (2021).
[27] A. Nelson, T. Neupert, A. Alexandradinata, and T. Bzdušek, Delicate topology protected by rotation symmetry: Crystalline Hopf insulators and beyond, Phys. Rev. B **106**, 075124 (2022).
[28] The key difference between our construction and those applied to rotation-symmetry preserving Hopf insulators [27,29] is the requirement that u_3 transform under the B representation of $\mathcal{C}^z_m$. Requiring the latter forces $u_3 = 0$ on the rotation axis. Consequently, the condition for band crossing, $u_4^2 = |\nu_3|$, is satisfied without fine tuning.
[29] J. E. Moore, Y. Ran, and X.-G. Wen, Topological surface states in three-dimensional magnetic insulators, Phys. Rev. Lett. **101**, 186805 (2008).
[30] See Supplemental Material at http://link.aps.org/supplemental/10.1103/PhysRevB.109.L081101 for a comparison with other models of Weyl semimetals; computational details of monopole and dipole flux; properties of 1D winding numbers.
[31] X. Zhang, J. Xia, Y. Zhou, D. Wang, X. Liu, W. Zhao, and M. Ezawa, Control and manipulation of a magnetic skyrmionium in nanostructures, Phys. Rev. B **94**, 094420 (2016).
[32] J. C. Y. Teo, L. Fu, and C. L. Kane, Surface states and topological invariants in three-dimensional topological insulators: Application to $Bi_{1-x}Sb_x$, Phys. Rev. B **78**, 045426 (2008).
[33] B. A. Bernevig, T. L. Hughes, and S.-C. Zhang, Quantum spin Hall effect and topological phase transition in HgTe quantum wells, Science **314**, 1757 (2006).
[34] W. P. Su, J. R. Schrieffer, and A. J. Heeger, Solitons in polyacetylene, Phys. Rev. Lett. **42**, 1698 (1979).
[35] A. C. Tyner, S. Sur, D. Puggioni, J. M. Rondinelli, and P. Goswami, Topology of three-dimensional Dirac semimetals and quantum spin Hall systems without gapless edge modes, Phys. Rev. Res. **5**, L012019 (2023).
[36] E. Prodan, Robustness of the spin-Chern number, Phys. Rev. B **80**, 125327 (2009).
[37] K.-S. Lin, G. Palumbo, Z. Guo, J. Blackburn, D. P. Shoemaker, F. Mahmood, Z. Wang, G. A. Fiete, B. J. Wieder, and B. Bradlyn, Spin-resolved topology and partial axion angles in three-dimensional insulators, Nat. Commun. **15**, 550 (2024).
[38] Q. Wei, X. Zhang, W. Deng, J. Lu, X. Huang, M. Yan, G. Chen, Z. Liu, and S. Jia, Higher-order topological semimetal in acoustic crystals, Nat. Mater. **20**, 812 (2021).
[39] Z. Yan, Higher-order topological odd-parity superconductors, Phys. Rev. Lett. **123**, 177001 (2019).
[40] S. Sur, A. C. Tyner, and P. Goswami, Mixed-order topology of Benalcazar-Bernevig-Hughes models, arXiv:2201.07205.
[41] B. J. Wieder, Z. Wang, J. Cano, X. Dai, L. M. Schoop, B. Bradlyn, and B. A. Bernevig, Strong and fragile topological Dirac semimetals with higher-order Fermi arcs, Nat. Commun. **11**, 627 (2020).
[42] X.-L. Qi and S.-C. Zhang, Spin-charge separation in the quantum spin Hall state, Phys. Rev. Lett. **101**, 086802 (2008).
[43] Y. Ran, A. Vishwanath, and D.-H. Lee, Spin-charge separated solitons in a topological band insulator, Phys. Rev. Lett. **101**, 086801 (2008).
[44] A. Mesaros, R.-J. Slager, J. Zaanen, and V. Juričić, Zero-energy states bound to a magnetic π-flux vortex in a two-dimensional topological insulator, Nucl. Phys. B **867**, 977 (2013).
[45] V. Juričić, A. Mesaros, R.-J. Slager, and J. Zaanen, Universal probes of two-dimensional topological insulators: Dislocation and π flux, Phys. Rev. Lett. **108**, 106403 (2012).
[46] A. C. Tyner, S. Sur, Q. Zhou, D. Puggioni, P. Darancet, J. M. Rondinelli, and P. Goswami, Quantized Non-Abelian, Berry's flux and higher-order topology of Na_3Bi, arXiv:2102.06207.
[47] Z. Wang and P. Zhang, Quantum spin Hall effect and spin-charge separation in a kagomé lattice, New J. Phys. **12**, 043055 (2010).
[48] A. C. Tyner and P. Goswami, Spin-charge separation and quantum spin Hall effect of β-bismuthene, Sci. Rep. **13**, 11393 (2023).
[49] X.-X. Yuan, L. He, S.-T. Wang, D.-L. Deng, F. Wang, W.-Q. Lian, X. Wang, C.-H. Zhang, H.-L. Zhang, X.-Y. Chang, and L.-M. Duan, Observation of topological links associated with Hopf insulators in a solid-state quantum simulator, Chin. Phys. Lett. **34**, 060302 (2017).
[50] D.-L. Deng, S.-T. Wang, K. Sun, and L.-M. Duan, Probe knots and Hopf insulators with ultracold atoms, Chin. Phys. Lett. **35**, 013701 (2018).
[51] C.-R. Yi, J.-L. Yu, W. Sun, X.-T. Xu, S. Chen, and J.-W. Pan, Observation of the Hopf links and Hopf fibration in a 2D topological Raman lattice, arXiv:1904.11656.
[52] T. Schuster, F. Flicker, M. Li, S. Kotochigova, J. E. Moore, J. Ye, and N. Y. Yao, Realizing Hopf insulators in dipolar spin systems, Phys. Rev. Lett. **127**, 015301 (2021).
[53] T. Schuster, F. Flicker, M. Li, S. Kotochigova, J. E. Moore, J. Ye, and N. Y. Yao, Floquet engineering ultracold polar molecules to simulate topological insulators, Phys. Rev. A **103**, 063322 (2021).
[54] F. N. Ünal, A. Eckardt, and R.-J. Slager, Hopf characterization of two-dimensional floquet topological insulators, Phys. Rev. Res. **1**, 022003(R) (2019).
[55] Z. Wang, X.-T. Zeng, Y. Biao, Z. Yan, and R. Yu, Realization of a Hopf insulator in circuit systems, Phys. Rev. Lett. **130**, 057201 (2023).
[56] D.-L. Deng, S.-T. Wang, C. Shen, and L.-M. Duan, Hopf insulators and their topologically protected surface states, Phys. Rev. B **88**, 201105(R) (2013).
[57] M. Ezawa, Topological semimetals carrying arbitrary Hopf numbers: Fermi surface topologies of a Hopf link, Solomon's knot, trefoil knot, and other linked nodal varieties, Phys. Rev. B **96**, 041202(R) (2017).
[58] A. Graf and F. Piéchon, Massless multifold Hopf semimetals, Phys. Rev. B **108**, 115105 (2023).
[59] P. Zhu, A. Alexandradinata, and T. L. Hughes, $\mathbb{Z}_2$ spin Hopf insulator: Helical hinge states and returning Thouless pump, Phys. Rev. B **107**, 115159 (2023).